



OPEN Multi-objective optimization of multiple droplet impacts on a molten PCM using NSGA-II optimizer and artificial neural network

Shahin Faghiri¹, Parham Poureslami¹, Hadi Partovi Aria² & Mohammad Behshad Shafii^{1,3✉}

Embracing an interaction between the phase change material (PCM) and the droplets of a heat transfer fluid, the direct contact (DC) method suggests a cutting-edge solution for expediting the phase change rates of PCMs in thermal energy storage (TES) units. In the direct contact TES configuration, when impacting the molten PCM pool, droplets evaporate, provoking the formation of a solidified PCM area (A). Then, they reduce the created solid temperature, leading to a minimum temperature value (T_{min}). As a novelty, this research intends to maximize A and minimize T_{min} since augmenting A expedites the discharge rate, and by lowering T_{min} , the generated solid is preserved longer, resulting in a higher storage efficacy. To take the influences of interaction between droplets into account, the simultaneous impingement of two ethanol droplets on a molten paraffin wax is surveyed. Impact parameters (Weber number, impact spacing, and the pool temperature) govern the objective functions (A and T_{min}). Initially, through high-speed and IR thermal imaging, the experimental values of objective functions are achieved for a wide range of impact parameters. Afterward, exploiting an artificial neural network (ANN), two models are fitted to A and T_{min} , respectively. Subsequently, the models are provided for the NSGA-II algorithm to implement multi-objective optimization (MOO). Eventually, utilizing two different final decision-making (FDM) approaches (LINMAP and TOPSIS), optimized impact parameters are attained from the Pareto front. Regarding the results, the optimum amount of Weber number, impact spacing, and pool temperature accomplished by LINMAP and TOPSIS procedures are 309.44, 2.84 mm, 66.89 °C, and 294.98, 2.78 mm, 66.89 °C, respectively. This is the first investigation delving into the optimization of multiple droplet impacts for TES applications.

List of symbols

\bar{A}	Dimensionless solidified PCM area ($\bar{A} = \frac{A}{\pi D^2}$)
A	Solidified PCM area (mm ²)
c_p	Specific heat capacity (kJ/kgK)
D	Initial droplet diameter (mm)
\bar{d}_h	The dimensionless horizontal impact spacing ($\bar{d}_h = \frac{d_h}{D}$)
d_h	Horizontal impact spacing (mm)
H	Falling height (cm)
T	PCM pool temperature (°C)
T_{min}	Minimum pool temperature value after the impact (°C)
T_s	Paraffin solidification point (°C)
t	Characteristic time (s)

¹Department of Mechanical Engineering, Sharif University of Technology, Tehran, Iran. ²School of Mechanical Engineering, College of Engineering, University of Tehran, Tehran, Iran. ³Sharif Energy, Water and Environment Institute (SEWEI), Tehran, Iran. ✉email: behshad@sharif.edu

v	Impact velocity (m/s)
We	Weber number $\left(We = \frac{\rho v^2 D}{\sigma}\right)$

Greek letters

β	The tilted angle of the high-speed camera ($^\circ$)
θ	Dimensionless temperature $\left(\theta = \frac{T}{T_s}\right)$
θ_{min}	Dimensionless minimum pool temperature value after the impact $\left(\theta_{min} = \frac{T_{min}}{T_s}\right)$
ρ	Ethanol density (kg/m ³)
σ	Ethanol surface tension (N/m)

Abbreviations

ANN	Artificial neural network
DC	Direct contact
FFNN	Function fitting neural network
HTF	Heat transfer fluid
IBF	Intermediate boiling fluid
IR	Infrared radiation
LHTES	Latent heat thermal energy storage
LINMAP	Linear programming technique for multi-dimensional analysis of performance
MOO	Multi-objective optimization
MSE	Mean squared error
NSGA II	Non-determined sorting genetic algorithm II
TES	Thermal energy storage
TOPSIS	Technique of order performance by similarity to an ideal solution

With an eye to diminishing carbon production, renewable energies have gained painstaking attention. However, variations in the supply of renewable energies have become a ubiquitous challenge, making thermal energy storage (TES) a consequential research topic¹. In fact, TES plays a pivotal role in renewable energies as it bridges the gap between power supply and its requirement over the course of peak hours.

Among disparate approaches for storing thermal energy, latent heat thermal energy storage (LHTES) is of great significance and applicability by virtue of its noticeable storage capacity^{2,3}. Phase change materials (PCMs) are extensively exploited in LHTES in view of not only high latent heat but trivial temperature changes during the phase change processes. Moreover, PCMs are widely employed in solar energy systems⁴, buildings^{5,6}, desalination⁷, and thermal management of electronic devices⁸. However, the inherent defect of PCMs, low thermal conductivity, prolongs their melting (charge) and solidification (discharge) processes, restricting their applications. Metal foams⁹, expanded graphite^{10,11}, nanoparticles^{12,13}, or a combination of them^{14,15} have been widely utilized to enhance the thermal conductivity of PCMs. Applying the direct contact (DC) between the PCM and heat transfer fluid (HTF) is another innovative solution by which the heat transfer efficiency of PCMs may be critically enhanced, accelerating the melting and, notably, solidification procedures¹⁶.

Martin et al.¹⁷ employed the DC procedure to store cold. They asserted that flow rate, temperature difference, and droplet size are prevailing factors controlling the discharge process. Ameliorating heat transfer and sustainability performance, Hegner et al.¹⁸ investigated a direct contact LHTES system, employing ester as the PCM. They claimed that flowing HFT through the PCM results in tiny droplets, which improve the effective heat transfer area. Furthermore, they concluded that all melting and solidification processes lasted less than an hour despite their unoptimized system. Al Omari et al.¹⁹ scrutinized the influences of vibrations on the DC heat transfer between hot water and a heat sink comprised of a PCM. Comparing the results obtained under vibrations and static conditions, they observed a sharp enhancement in the cooling rate of hot water when the vibrational effects were brought to bear. Nonetheless, as the authors declared, further optimizations may be expected to improve the system's efficacy. Hosseinaveh et al.²⁰ appreciably precipitated the charge and discharge rates of PCMs through the DC method, in which the HTF (acetone) boils within the paraffin and takes heat from it, bringing about the PCM solidification and HTF evaporation. Then, the acetone vapor condenses in the condenser, leading to numerous tiny HTF droplets. Following this, acetone droplets impinge on the surface of molten paraffin. The process continues so that the PCM is exhaustively solidified. They also indicated that, under the optimum situation, this approach strikingly lessens the discharge, charge, and total charging-discharging times. Utilizing the DC method between the HTF and PCM, Ramezani et al.²¹ decreased the overall discharge rate of PCMs from 2 h to 39 s. Similar to the previous scholarship, acetone droplets formed on the condenser impacted the molten PCM and caused it to solidify. Accordingly, the DC technique, through which the trouble of PCMs' slow discharge rate is ironed out, encompasses an interaction between the PCM and HTF droplets. This investigation strives to optimize the droplets' impact parameters and characterize the circumstances under which the PCMs' discharge rate is further expedited in novel TES devices.

Disregarded in most surveys due to its sophistication, multiple droplet impacts (simultaneous, non-simultaneous, and successive) on liquid films, liquid pools, and solid surfaces have numerous applications, including spray cooling²², inkjet printing²³, spray coating²⁴, desalination²⁵, and so forth. Liang et al.²⁶ studied the simultaneous and non-simultaneous impact of a droplet pair at room temperature. According to their investigation, high Weber numbers (We) result in a central liquid sheet, which is a three-dimensional phenomenon. Moreover, increasing droplet vertical spacing (or time lag between droplets) in the

non-simultaneous case brings about a decline not only in central liquid sheet height but in the spreading factor. They also found that the influence of vertical spacing declines as the We number increases. Employing the volume of fluid approach, Guggilla et al.²⁷ studied the hydrodynamic and heat transfer characteristics of drop-on-drop impact on a hot surface. They maintained that the We number, Bond number, and Jakob number have an overriding influence on the spreading factor and evaporation dynamics of droplet impact. Guilizzoni et al.²⁸ numerically surveyed multiple droplets simultaneously impacting the deep pool utilizing OpenFOAM® software. The results demonstrate that by increasing the impact spacing between droplets, the time evolution of craters would resemble that of a single droplet. Moreover, the shorter the impact spacing, the deeper the crater. Goswami and Hardalupas²⁹ concentrated on the simultaneous impingement of two droplets on a dry surface. They claimed that the secondary droplets provoked by the uprising sheet splash are larger than those caused by a single droplet impingement. Kirar et al.³⁰ experimentally examined the impact of two ethanol droplets on the ethanol pool at low impact velocity. They found that when the normalized distance between the droplet exceeds 3.2, the interaction between neighboring capillary waves is undermined, ending up with a partial coalescence. Generally speaking, there are overly few studies in the literature concentrating on the multiple droplet impact hydrodynamics and heat transfer.

Optimization is of great momentousness in the design of systems in light of its capability to address complex and practical problems³¹. As the term suggests, optimization refers to the process of finding the best values for an objective function based on a set of parameters. Single-objective optimization, in which only one objective function is considered, has a unique Pareto optimal solution. In contrast, multi-objective optimization (MOO)³² expands the idea of optimization by enabling the concurrent optimization of several individual objectives. MOO is a mathematical methodology that discovers diverse possibilities, all representing the optimal Pareto solution.³³ Conducting MOO to minimize the PCM phase change time and maximize the exergy conversion, Zhang et al.³⁴ suggested a combination of nanoparticles, metal foam, heat pipe, and fin to boost the efficacy of an LHTES unit. Taking heat transfer effectiveness and PCM melting time as the objective functions, Lin et al.³⁵ performed MOO for a TES system. They raised heat transfer effectiveness by 34.0%. Huang et al.³⁶ proposed a MOO method utilizing a genetic algorithm to reduce entropy generation and the upfront cost of geothermal ground heat exchangers. They lessened the operation cost of the system by 9.5%. Liang et al.³⁷ explored the influences of PCM heat transfer improvement and geometric optimization on the overall storage performance. The results reveal that increasing the ratio of tube length to tube diameter instigates an increment in the effective energy storage ratio. Peng et al.³⁸ conducted numerical optimization of patterned metal fins by adjusting their dimensions to optimize the convection-controlled and conduction-controlled regions during the charging process. The results demonstrated significant improvements in charging performance, which ranged from 42.7% to 63.7%, depending on the optimization arrangement and heating temperature. Given the literature, there are few surveys on the optimization of TES systems composed of PCM³⁹. Also, few studies have been focused on optimizing the droplet impact process⁴⁰, entailing researchers to accomplish thorough investigations in this field. Moreover, no study has been conducted to optimize the impact parameters of liquid droplets so that the phase change time of the PCM is reduced.

In conclusion, the continuous impact of multiple HTF droplets on the PCM surface in the DC technique, solidifying the entire PCM expeditiously, provides an ingenious solution for the PCMs' meager thermal conductivity. As a representative of genuine DC energy storage units, the simultaneous impingement of a droplet pair on the PCM surface is considered here so that the interaction between neighboring droplets can also be taken into account. Once impacting the molten PCM pool, droplets absorb heat from the pool and evaporate, which solidifies a portion of the paraffin and lessens its temperature. Thus, in this research, solidified PCM area (A) and the minimum pool temperature value after the impact (T_{\min}) are the objective functions characterized by high-speed and IR thermal imaging, respectively. Three design parameters affecting the objective functions are the We number, horizontal impact spacing (d_h), and the PCM temperature before the impact (T). As a novelty, a MOO is implemented in this scholarship to characterize the impact conditions by which A is maximized, while T_{\min} is minimized, which engenders a more sizeable and more stable solid, leading to a more expeditious charge and discharge processes (see Section "Experimental results"), which has been the main stimulant for conducting the research. To put it another way, the study strives to enhance the effectiveness of a TES unit working based on the direct contact between HTF and PCM, which is its primary significance. In this survey, the following stages are performed, respectively:

1. Immense experiments are conducted systematically for various design parameters so that the experimental values of the objective functions (A and T_{\min}) are procured.
2. Experimental data are employed to train the artificial neural network (ANN) to obtain two models for the objective functions.
3. The trained network is given to the multi-objective non-dominated sorting genetic algorithm II (NSGA-II) to accomplish MOO.
4. Eventually, the optimum impact conditions are attained from the Pareto front by final decision-making (FDM) approaches.

Multiple droplet impingement is an intricate phenomenon, which is largely due to the interaction between adjacent droplets; therefore, investigations allocated to this challenging topic are rare compared to studies surveying the single droplet impact. Hence, delving into the simultaneous impact of a droplet pair is one of the novelties of the research. Additionally, studies investigating multiple droplet impacts on a liquid pool are scarce. Also, intriguingly, this investigation embraces two simultaneous phase changes (i.e., paraffin solidification and ethanol droplet evaporation, which has not been explored previously. Moreover, to the best of the authors'

knowledge, there is no research in the literature concentrating on the optimization of droplet impact parameters for TES applications.

Experimental method

Selecting PCM and HTF. Paraffin wax was employed as the PCM due to its low cost, abundance, non-toxicity as well as high latent heat. The latent heat of paraffin and its phase change point were attained by the DSC experiment, whose results are shown in Fig. 1. Based on Fig. 1, the PCM solidification peak is 66.89 °C. Furthermore, the PCM's thermal conductivity was specified by a KD2 pro instrument. Throughout the text, the terms PCM and paraffin are used interchangeably.

In the DC technique, the fluid saturation point should be lower than the PCM temperature; therefore, once contacting the PCM, the fluid evaporates and absorb heat from the paraffin so that the entire paraffin is solidified. Moreover, the HTF should be insoluble in the liquid PCM. Additionally, the density of PCM and HTF should be sufficiently different, making the separation between them uncomplicated¹⁷. Complying with the mentioned points, ethanol 96% was picked out as HTF for producing the droplets. Tables 1 and 2 summarize the properties of ethanol and PCM, respectively. It should be mentioned that the DSC analysis was also conducted for ethanol and paraffin mixture, whose results indicated that ethanol did affect paraffin properties negligibly as the ethanol is essentially insoluble in paraffin.

Since the paraffin temperature is higher than the ethanol saturation point, ethanol boils inside the PCM and subsequently evaporates; hence, the mode of heat transfer will be boiling whose heat transfer coefficient is sharply greater than convection; thus, applying a direct contact between the ethanol and paraffin may result in an exceeding increase in the melting and solidification rates of PCMs, which is desirable in TES, where paraffin is utilized as the storage material. Furthermore, DC heat transfer between ethanol and paraffin is useful for applications where the rates of charge and discharge should be monitored, which may be simply accomplished by varying the PCM to heat transfer HTF ratio. Also, this approach may be advantageous to cooling systems in which there is a limitation for the size of the system. Since the time of melting and solidification is overly short due to the high heat transfer rate caused by the boiling of HTF inside the PCM, numerous charge–discharge cycles may be fulfilled in a limited time, compensating for the low system size.

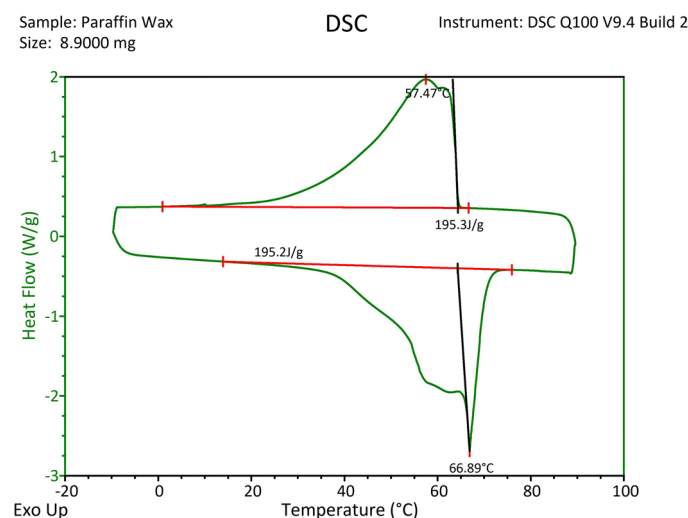


Figure 1. DSC analysis of granular paraffin wax, utilized as the PCM in the present study.

Saturation point (°C)	Enthalpy of evaporation (kJ/kg)	σ (N/m)	μ (Pa.s)	ρ (kg/m ³)	c_p (kJ/kgK)
78.5	846.0	0.02255	0.0012	785	2.46

Table 1. Ethanol 96% properties.

Solidification point (°C)	Enthalpy of fusion (kJ/kg)	Thermal conductivity at 80 °C (W/mK)	c_p at the liquid phase (kJ/kgK)
66.89	158.5	0.227	2.4

Table 2. Paraffin wax properties.

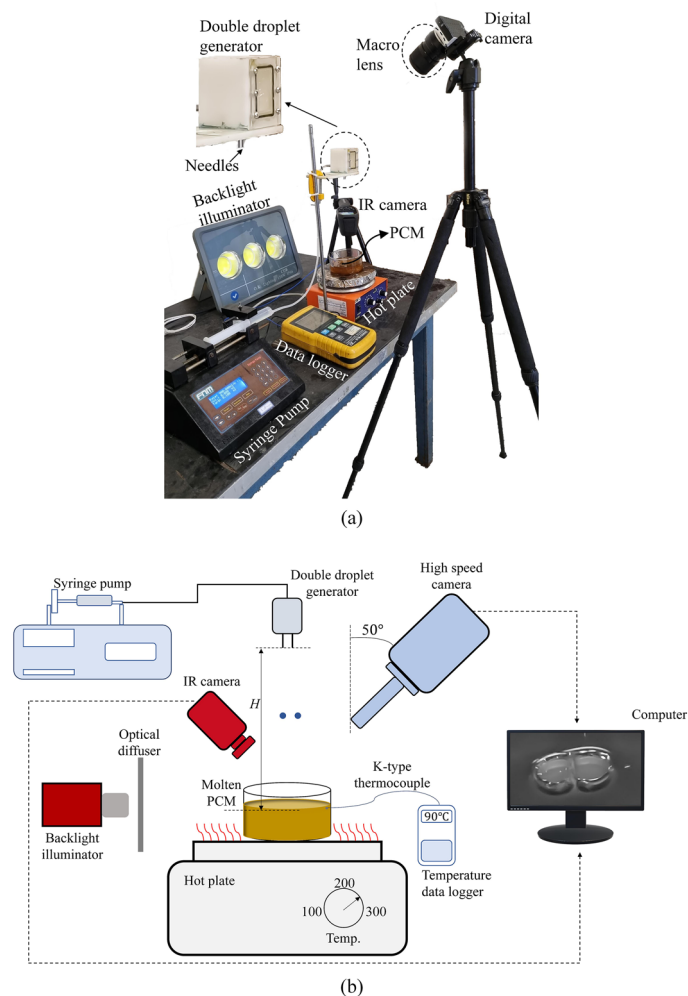


Figure 2. Experimental setup; (a) real image, and (b) schematic diagram.

Experimental setup. Figure 2 demonstrates the experimental setup along with its schematic diagram. Initially, heated by a hot plate, paraffin reached a specific temperature (70, 75, 80, 85, 90, 95 °C), which was measured invariably using calibrated K-type thermocouples, connected to a data logger (BTM-4208SD). Then, the hot plate was deactivated. At this stage, by exerting a tiny force on a syringe utilizing a syringe pump, an ethanol droplet pair was separated from needles located at the height H (10, 15, 20, 25 cm). By varying the droplet release height (H), the impact velocity may be changed, which affects the Weber number (see Section "Image post processing"). Hence, the effects of the Weber number on the objective functions are examined by changing H . The values of H were chosen so that a wide variety of droplet impact dynamics is taken into account⁴¹; therefore, a comprehensive data set was exploited to train the artificial neural network. Furthermore, the H values were selected according to a TES unit performing based on the DC approach²⁰. For droplet pair generation, two blunt-tip needles with an inner diameter of 1.6 mm were attached to the droplet generator. To survey the horizontal spacing effects on the objective functions, four droplet generator devices were constructed in which the distance between needles' centers varies from 4.02 to 12.06 mm. Equipped with a Macro lens for magnification, a digital CMOS camera (Nikon 1 J4) was fixed 50° with respect to the vertical axis so that the PCM surface could be captured. To capture the details of the multiple droplet impact phenomenon, the digital camera shooting rate was set to 1200 Hz with 416 × 144 pixels in each image in which each pixel roughly corresponds to 0.11 mm (the calibration was conducted by an object with determinate dimensions). Moreover, having a resolution of 640 × 480 pixels, an IR camera (Seek Thermal) was employed to investigate the paraffin surface temperature distribution after the impingement. To carry out the shadowgraph method, an LED light source was used. In addition, an optical diffuser was used to monotonously diffuse the light. The paraffin container, whose outer diameter is 100 mm, has been constructed from Pyrex. Furthermore, the container's dimensions were selected such that walls would not affect the impact dynamics⁴². The PCM height in the container was fixed at 30 mm in all experiments as well. Though ethanol is insoluble in paraffin and evaporates after the droplet impact, the paraffin was completely altered after each experiment to avoid any PCM thermal degradation and exclude the effects of ethanol on the paraffin properties. An exhaustive elucidation of the experimental setup has been provided in our previous research⁴¹.

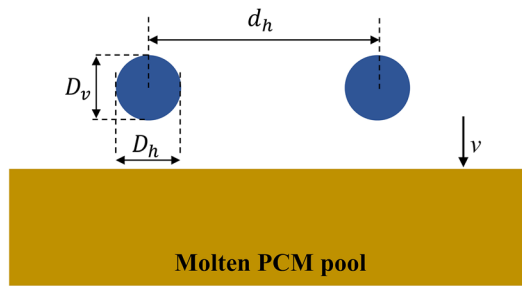


Figure 3. Defining impact parameters.

Image post processing. Impact velocity and initial droplet diameter were determined by pixel analyzing of the images. The initial droplet diameter was calculated as follows⁴³:

$$D = (D_h^2 D_v)^{\frac{1}{3}} \quad (1)$$

where D_v and D_h are the vertical and horizontal axes of the droplets as indicated in Fig. 3. Since droplets do not maintain a spherical shape during falling, D_v and D_h are not the same. By employing Eq. (1), the droplet diameter equals 2.68 ± 0.2 mm. Herein, the droplet diameter is supposed to be 2.68 mm for all experiments. The droplet impact velocity was obtained as follows:

$$v = \frac{\Delta y}{\Delta t} \quad (2)$$

where Δy is the droplet displacement in the y -direction just before the impact, and Δt is the time difference between the two successive images. It should be expressed that for computing the impact velocity and droplet diameter, the high-speed camera was fixed at 0° .

Additionally, the We number can be calculated as follows:

$$We = \frac{\rho v^2 D}{\sigma} \quad (3)$$

where D is the initial droplet diameter, ρ and σ are the ethanol density and surface tension, respectively, as given in Table 1. The experimental and theoretical impact velocities based on four falling heights (H) used in the study are provided in Table 3. Regarding Table 3, it is axiomatic that theoretical and experimental results are in apt agreement with the average error below 1%. Moreover, the impact nomenclature is schematically illustrated in Fig. 3, in which d_h represents horizontal impact spacing and varies between 4.02 and 12.06 mm, as mentioned above. This parameter is nondimensionalized by the droplet diameter as follows⁴⁴:

$$\bar{d}_h = \frac{d_h}{D} \quad (4)$$

where \bar{d}_h is defined as dimensionless horizontal spacing, whose values alter from 1.5 to 4.5.

Generated after two ethanol droplets impacting the paraffin surface, the solidified PCM area was determined by DMV software⁴⁵, whose procedure is shown in Fig. 4. In the first stage, Fig. 4c, background subtraction was accomplished, accentuating the desired area. Subsequently, demonstrated in Fig. 4d, the grayscale image was converted to an 8-bit binary image via a user-defined threshold. At this step, the boundaries of the area were recognized. Then, minuscule erroneous objects, created in previous stages unintentionally (see Fig. 4d), were eliminated by a threshold, as shown in Fig. 4e. The border of the image can be omitted at this stage as well. Eventually, the fill holes option filled the gaps inside the region, ending up producing a well-defined zone whose area could be identified (Fig. 4f). The final values achieved from DMV were corrected by dividing $\cos(\beta)$, in which β is the tilted angle of the high-speed camera ($\beta = 50^\circ$).

H (cm)	v_{exp} (m/s)	$v_{theory} (\sqrt{2gH}, m/s)$	We
10	1.38	1.40	179
15	1.71	1.72	275
20	1.99	1.98	373
25	2.21	2.21	464

Table 3. Experimental and theoretical impact velocity along with the We number based on four different falling heights used in this study.

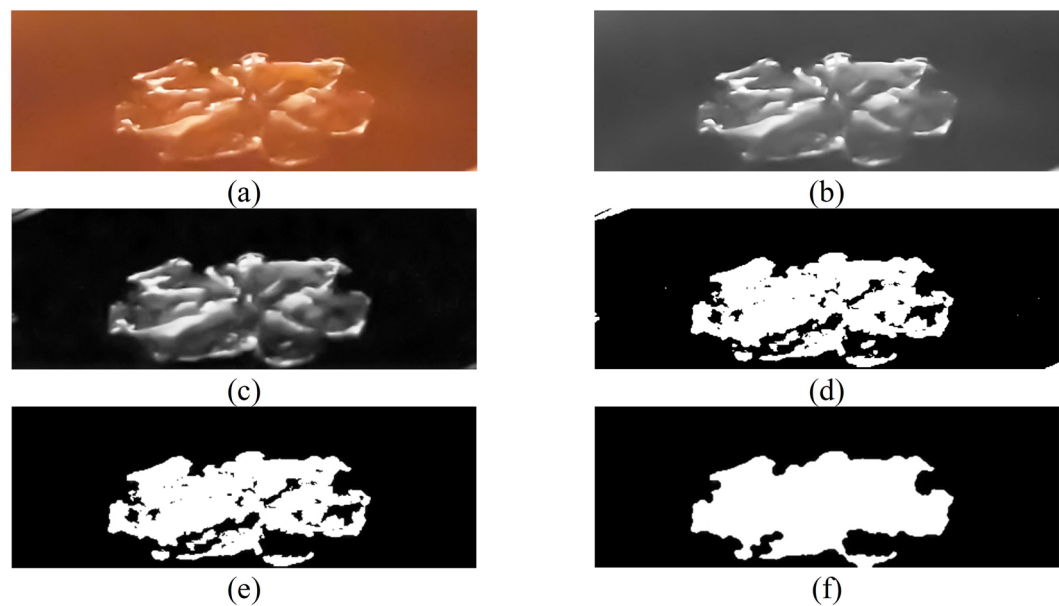


Figure 4. The post-processing stages implemented to determine the solidified PCM area; (a) original image, (b) grayscale image, (c) background subtraction, (d) binarized image and the edge diagnosis, the incorrect object that is occurred in the top left of the figure is unequivocal, (e) eliminating the tiny incorrect object happened in the previous step, and (f) the final image after filling the gaps; the area is calculated by this image. The impact conditions are $We = 373$, $d_h = 2.5$, and $T = 70$ °C.

Uncertainty analysis. Inevitable errors in the current investigation chiefly originate from the measurement of the PCM temperature and droplet impact velocity. The paraffin temperature prior to the impact was attained by a k-type thermocouple, whose accuracy was 0.5 °C. Furthermore, the temperature distribution of the PCM surface was determined by an IR camera having an accuracy of 0.3 °C. In addition, data post-processing was implemented with an accuracy of 1 pixel, which corresponds to a 0.11 mm error. Thus, given the shooting rate of the camera (1200 fps), the impact velocity was calculated with an accuracy of 0.13 m/s. Based on Taylor's theory, the uncertainty in the Weber number is as follows⁴⁶:

$$\frac{\delta We}{We} = \sqrt{\left(\frac{\delta D}{D}\right)^2 + \left(\frac{2\delta v}{v}\right)^2} \quad (5)$$

According to Eq. (5), the error in the Weber number calculation is, on average, 16.4% for different impact velocities. Table 4 recapitulates the accuracy of the experimental apparatus utilized in this survey.

Experimental results

Two influential phenomena take place in the wake of ethanol droplet impact on the PCM pool: 1- absorbing heat from the PCM, ethanol droplets commence evaporating, and 2- the molten PCM is solidified. A couple of objective functions playing a momentous role in describing the mentioned incidences are the PCM solidified area (A) and the minimum PCM pool temperature value after the impact (T_{\min}), which are actually representative of the latent and sensible heat. Three design parameters, i.e., PCM pool temperature (T), impact spacing (d_h), and We number influence the objective functions. The effect of these design parameters on objective functions will be scrutinized in this section. The experiments were carried out for four different We numbers (179, 275, 373, and 464), four different dimensionless impact spacing (1.5, 2.5, 3.5, and 4.5), and six various pool temperatures (70, 75, 80, 85, 90, and 95 °C); hence, a huge amount of experimental data (96 cases) was produced for the optimization purpose. To examine reproductivity and ensure accuracy, each case was repeated at least three times, and the presented data is the average of three cases.

Apparatus	Error
Syringe pump	1 μ l/h
High-speed camera	0.11 mm
k-type thermocouple	± 0.5 °C
IR camera	± 0.3 °C

Table 4. Uncertainty of experimental apparatus.

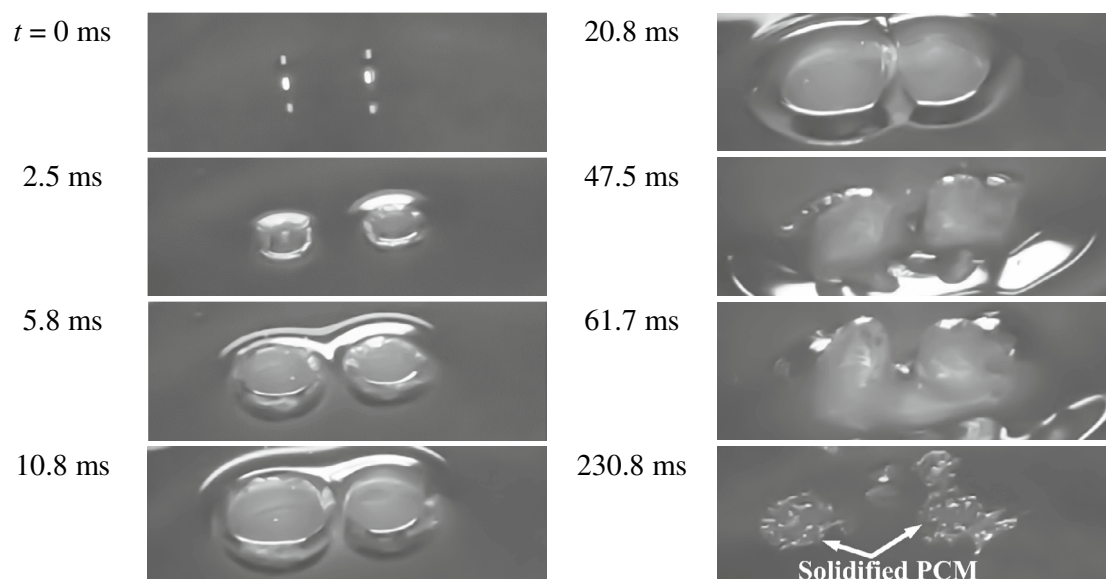


Figure 5. Time elapsed of solidified PCM area formation after simultaneous double droplet impact when $We = 464$, $\bar{d}_h = 3.5$, $T = 90^\circ\text{C}$.

The process of solid formation on the PCM surface is revealed in Fig. 5 for the impact condition of $We = 464$, $\bar{d}_h = 3.5$, and $T = 90^\circ\text{C}$, where $t = 0$ is the time at which the first droplet contact the PCM. Based on Fig. 5, craters are created shortly after the impingement ($t \approx 2.5$ ms); then, they expand vertically downward and radially until reach the maximum depth and width ($t \approx 20.8$ ms). When attaining maximum depth and width, craters rebound and two jets are ejected separately perpendicular to the paraffin surface ($t = 47.5$ ms), which evolve to achieve maximum height ($t \approx 61.7$ ms). Next, jets descend, and their heights diminish, ending up forming solidified PCM areas ($t = 230.8$ ms) on the pool surface. The detailed examination of impact dynamics is far beyond the scope of the present study.

PCM temperature effect. Figure 6 represents the influence of paraffin pool temperature (T) on the solidified PCM area (A) and the minimum pool temperature values after the impact (T_{\min}) for various We numbers at $\bar{d}_h = 2.5$. Based on Fig. 6a, it is obvious that A increases exceedingly as temperature diminishes for all We numbers. Indeed, when T is high, the major portion of heat extracted by ethanol droplets is sensible heat, lessening the paraffin temperature; therefore, the insignificant part of the absorbed heat is allocated to the PCM solidification, leading to a small solidified area. That is why the area at $T = 95^\circ\text{C}$ is quite small. Conversely, when the PCM temperature is sufficiently near to the freezing point, the remarkable portion of the heat absorbed by droplets is dedicated to the phase change and the negligible one is utilized to reduce the temperature up to the solidification point in the form of sensible heat, engendering a sizeable solidified area.

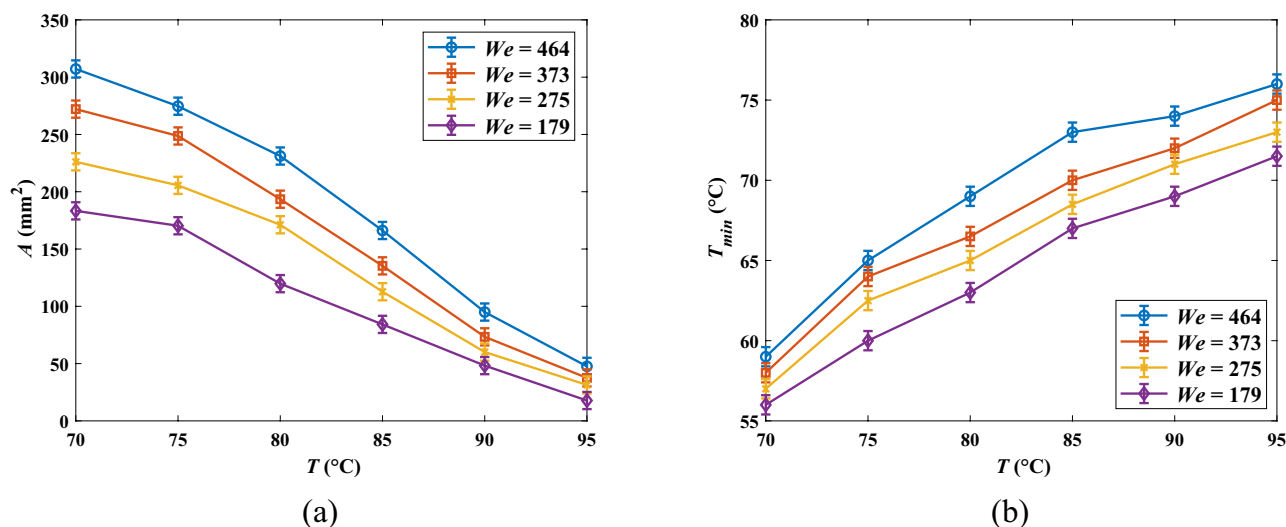


Figure 6. Solidified PCM area (A) and minimum pool temperature value after the impact (T_{\min}) as a function of PCM temperature (T) for different We numbers at $\bar{d}_h = 2.5$; (a) $A(T)$, and (b) $T_{\min}(T)$.

Moreover, regarding Fig. 6b, it is lucid that T_{\min} decreases when the pool temperature dwindles. At low pool temperatures, the chief part of the absorbed heat causes the phase change and curtails the created solid temperature well below the freezing point. In contrast, at high pool temperatures, T_{\min} is rather close to the phase change point, indicating that the solid zone can be wiped out promptly after the formation by absorbing heat from the pool, which is at a higher temperature. Consequently, not only does lessening the temperature provide a larger solidified area, but it reduces its temperature as well, which provokes a more “stable” solid region preserving for a longer period. In contrast, when T_{\min} is high, the created solid swiftly melts. It should be stated that although at $T = 95^\circ\text{C}$ minimum temperature value does not necessarily reach the solidification point of 66.89°C , the solidified PCM area was observed for this temperature since based on the DSC analysis the solidification process is actually initiated at about $T = 75^\circ\text{C}$ (see Fig. 1).

Figure 7 indicates the influence of PCM temperature on A for several pool temperatures when $We = 464$ and $\bar{d}_h = 3.5$. Unambiguously, the less the temperature, the more sizeable the solidified area. For instance, A at $T = 90^\circ\text{C}$ is 83.5 mm^2 , while that at $T = 80^\circ\text{C}$ is 218.7 mm^2 ; thus, an 11.1% reduction in temperature brings about a dramatic increment of 161.9% in A . Additionally, achieved by IR thermal imaging, Fig. 8 demonstrates the influence of pool temperature on T_{\min} in the mentioned impact conditions. As can be seen, the maximum temperature in each contour is slightly higher than the reported values of T since reported pool temperatures are indeed the average value measured by the thermocouple and slightly lower than the maximum temperature. Based on Fig. 8, by reducing the temperature from 75°C to 90°C , the minimum temperature is increased by roughly 11.0%.

Weber number effect. As indicated in Fig. 6a, augmenting We raises A for all pool temperature values. Actually, increasing the We number enhances the droplets’ inertia, which facilitates the spreading of the droplets onto the pool surface after the impact. Hence, the effective heat transfer surface between the PCM and the fluid is ameliorated, which instigates the solidified PCM area growth. For instance, A at $We = 275$ is, on average, 25.7% higher than that at $We = 179$. Additionally, scrutinizing the graphs of Fig. 6, one can figure out that the influence of We on A becomes weaker when the paraffin temperature diminishes. Increasing the viscosity due to the temperature decrement accounts for the phenomenon since growth in the viscosity boosts viscous dissipation, impeding droplet spreading on the surface, engendering a lower heat transfer area.

By contrast, given Fig. 6b, increasing the We number gives rise to a gain in T_{\min} , which is unfavorable in energy storage units. In fact, when the We number is low, droplets do not spread aptly on the PCM surface, reducing the pool-droplet interaction. Hence, in low We numbers, droplets interact with an insignificant portion of the paraffin surface, and their enthalpy of vaporization is devoted to solidification and lowering the temperature of a small area. Consequently, at low We numbers, droplets solidify a small region and then lessen its temperature remarkably, provoking a low T_{\min} . In contrast, at high We numbers, droplets interact with a notable part of the PCM, meaning that the evaporation of droplets is allotted to heat exchange with a larger PCM surface. Accordingly, as causing a phase change of a substantial area, the heat absorbed by the droplets is not adequate to diminish the solidified area’s temperature after the formation, engendering a higher T_{\min} . Accordingly, preserving for a longer time, the solid produced by low We numbers are more “stable” inasmuch as its temperature is far

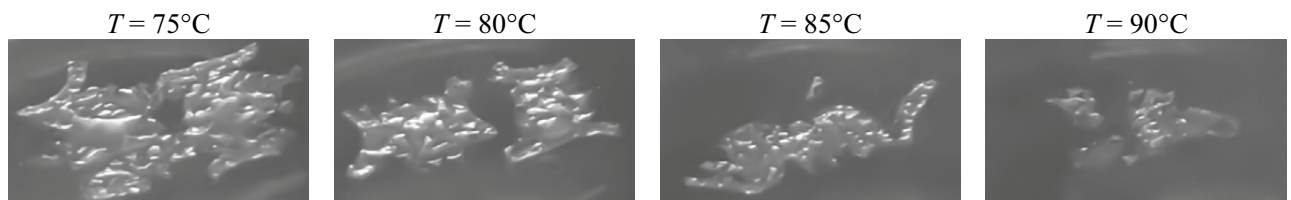


Figure 7. Solidified paraffin produced on the pool surface for various pool temperatures at $We = 373$ and $\bar{d}_h = 3.5$.

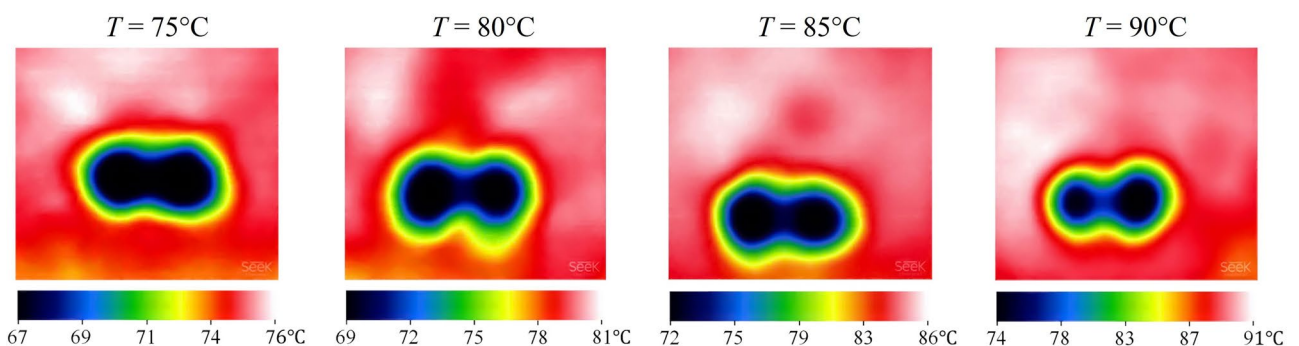


Figure 8. IR images of the PCM surface after the simultaneous impact of two droplets for various pool temperatures at $We = 373$ and $\bar{d}_h = 3.5$.

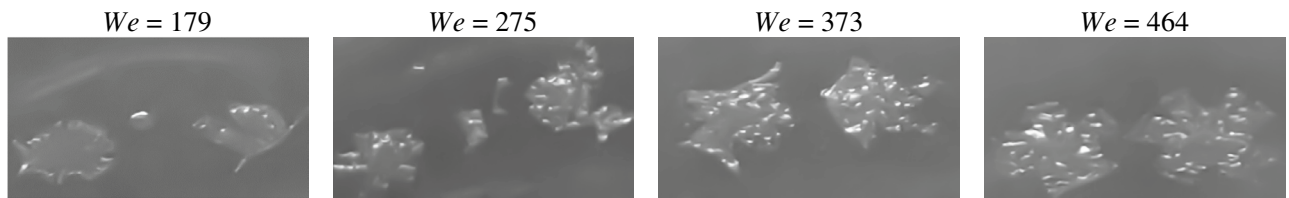


Figure 9. Solidified paraffin produced on the pool surface for various Weber numbers at $T = 85\text{ }^{\circ}\text{C}$ and $\bar{d}_h = 4.5$.

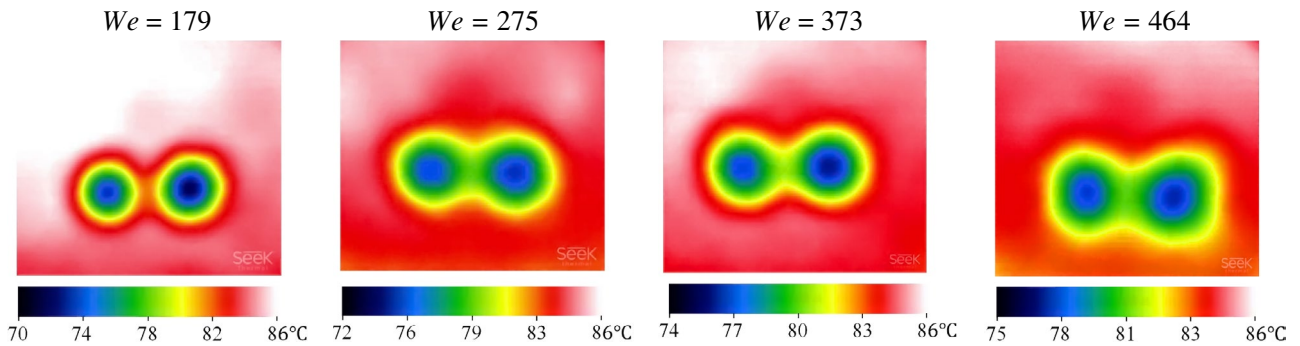


Figure 10. IR images of the PCM surface after the simultaneous impact of two droplets for various We numbers at $T = 85\text{ }^{\circ}\text{C}$ and $\bar{d}_h = 4.5$.

from the melting point. Conversely, being in higher temperatures, solidified PCM generated by high We number impacts have less stability and are annihilated shortly after the formation. This point is notably authentic when $T > 85\text{ }^{\circ}\text{C}$.

Figure 9 reveals the effect of We on A when $\bar{d}_h = 4.5$ and $T = 85\text{ }^{\circ}\text{C}$. At $We = 275$ the solidified PCM area is 146.4 mm^2 , while this value reaches 206.6 mm^2 for $We = 464$, implying that improving We by about 68.7% prompts a 41.1% enhancement in A . Figure 10 illustrates the temperature distribution of the paraffin surface after the impingement in similar impact conditions. According to Fig. 10, reducing the We number from 464 to 179 has led to a 7% decrement in T_{\min} . Moreover, the impingement region can be differentiated conveniently in all cases due to the noticeable temperature reduction that occurred in the wake of the impact. Additionally, regardless of the We number, the most efficient heat transfer region has occurred in the impact crater zone since T_{\min} has taken place in this region, which is consistent with Zhang et al.⁴⁷.

Impact spacing effect. Horizontal spacing has a consequential influence on the interaction between droplets, which in turn directly affects the objective functions of A and T_{\min} . Augmenting impact spacing substantially improves the solidified PCM area as demonstrated in Fig. 11a. Indeed, curtailing d_h strengthens the droplet–droplet interaction and attenuates the droplet–PCM interaction, which diminishes the spreading area of the droplets. Therefore, less fluid contact with the paraffin, and the effective heat transfer area lessens, instigating a decline in A . For instance, according to Fig. 11a, A at $\bar{d}_h = 3.5$ is, on average, 35% higher than that at $\bar{d}_h = 1.5$. Additionally, the effect of horizontal spacing on A diminishes as the temperature decreases since lessening the temperature intensifies paraffin surface tension, which hampers droplets spreading on the surface and lessens the heat transfer area between the droplets and the PCM.

Conversely, concerning Fig. 11b, T_{\min} is raised as the horizontal impact spacing increases, which is an undesirable factor in the TES system. At low impact spacing, since the spreading area is insignificant, droplets absorb heat from a small region of PCM, meaning that absorbed heat is dedicated to solidifying as well as lessening the temperature of a small zone. Consequently, in the case of shorter impact spacing, the created solid has a lower temperature. Hence, the shorter the impact spacing, the more stable the produced solid as it is maintained for a longer time.

The effect of horizontal spacing on the A is indicated in Fig. 12, in which $We = 464$ and $T = 85\text{ }^{\circ}\text{C}$. Vividly, increasing impact spacing has engendered a dramatic improvement in A . IR images of the PCM surface are displayed in Fig. 13 in the mentioned impact parameters. Regarding Fig. 13, the impingement zone for $\bar{d}_h = 1.5$ is smaller than that for $\bar{d}_h = 4.5$. Therefore, the sensible and latent heat of the droplets absorbed from the PCM is assigned to a tiny region that not only solidifies it but also reduces its local temperature exceedingly after the phase change. As a result, an insignificant solidified PCM area with a lower temperature is accomplished for the lower values of impact spacing. In addition, the heat transfer in the impact crater has the foremost efficacy since T_{\min} has occurred in this zone in all cases.

Figure 14 represents non-dimensional solidified area (\bar{A}) and non-dimensional minimum pool temperature value after the impact (θ_{\min}) as a function of non-dimensional impact spacing for different Weber numbers are provided in, in which $T = 90\text{ }^{\circ}\text{C}$. Evidently, \bar{A} grows when horizontal spacing is boosted. Furthermore, \bar{d}_h profiles shift upwardly as the We number is raised, indicating that the We number plays a critical role in the heat transfer

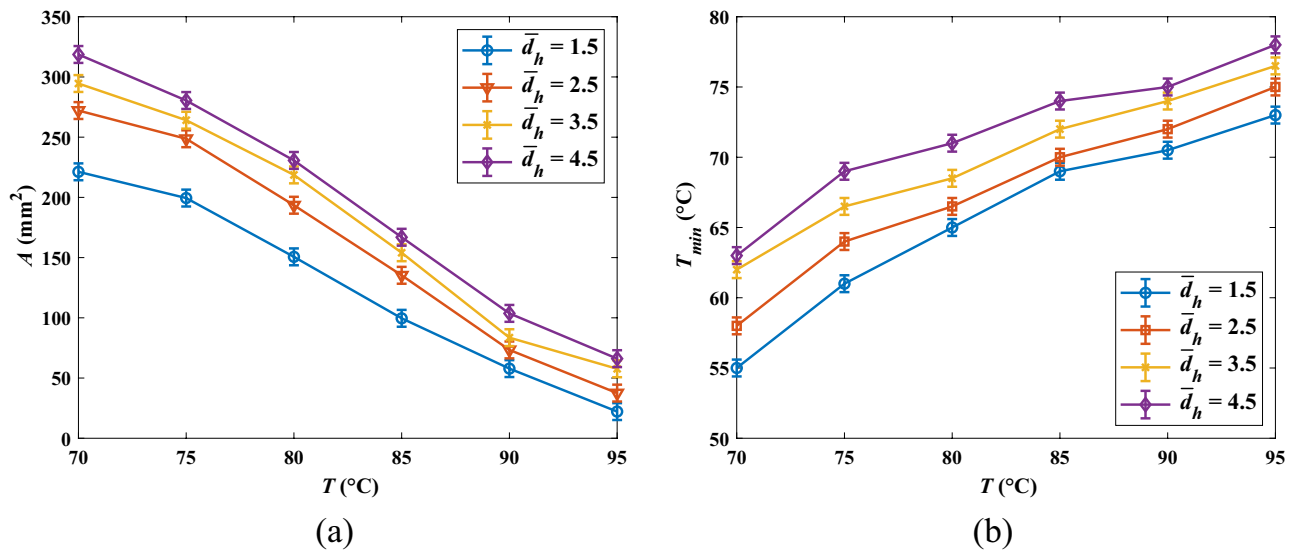


Figure 11. Variation of solidified PCM area (A) and minimum surface temperature (T_{\min}) against PCM temperature for four different horizontal impact spacing at $We = 373$; (a) $A(T)$, and (b) $T_{\min}(T)$.

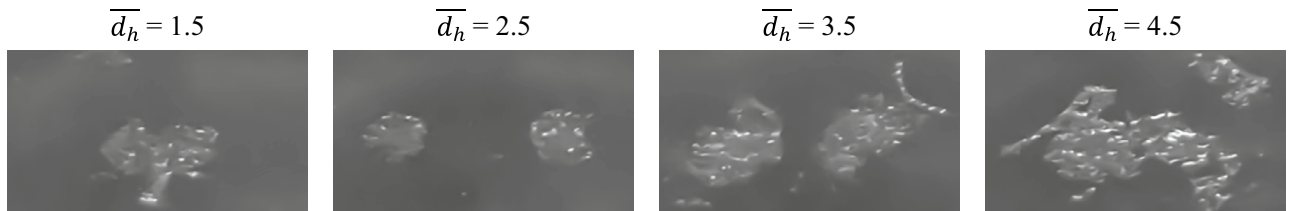


Figure 12. Solidified paraffin produced on the pool surface for various horizontal impact spacing at $We = 464$ and $T = 85^\circ\text{C}$.

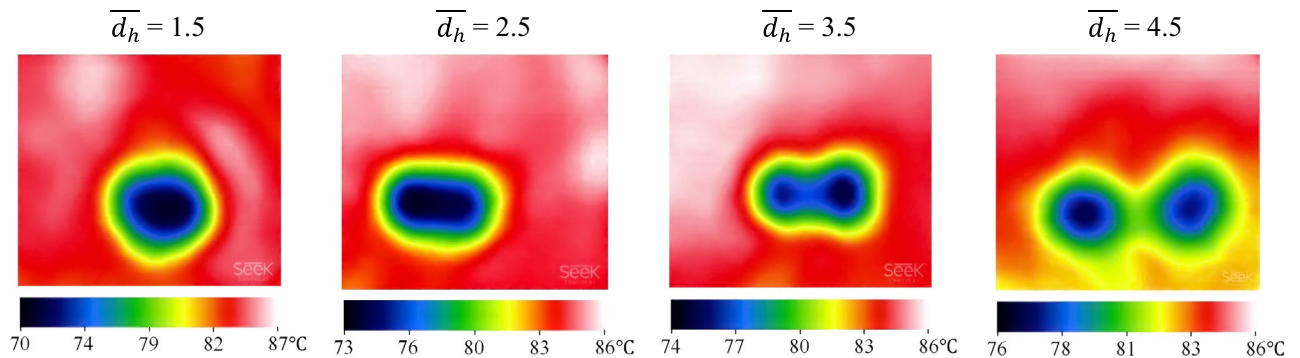


Figure 13. IR images of the PCM surface after the simultaneous impact of two droplets for various horizontal impact spacing at $We = 464$ and $T = 85^\circ\text{C}$.

characteristics of double droplet impingement. Therefore, as expected, the greatest \bar{A} value corresponds to $\bar{d}_h = 4.5$ and $We = 464$. On the other hand, θ increases as the We number and impact spacing grow, as described before.

Generally speaking, larger solids created on the pool after the impact are favorable in the DC approach as they hasten the discharge process; hence, more charge and discharge cycles can be achieved in a specific time. Moreover, the less T_{\min} , the more stable the solid. On the contrary, solids, whose temperatures are relatively high, are swiftly obliterated by absorbing heat from the molten PCM pool having a high temperature. Accordingly, the formation of a sizeable solid possessing a low temperature after the droplet impact is desirable in the DC procedure. However, as profoundly discussed in this section, though directly proportional to A , the Weber number and horizontal impact spacing are inversely proportional to T_{\min} . Therefore, by exploiting MOO, the current investigation strives to determine the optimum impact parameters through which A is maximized, and T_{\min} is minimized, which enhances the efficacy of the TES unit. Designed under this optimum condition, a system may take advantage of a low volume since numerous charge and discharge cycles conducted in a particular time can compensate for a small volume.

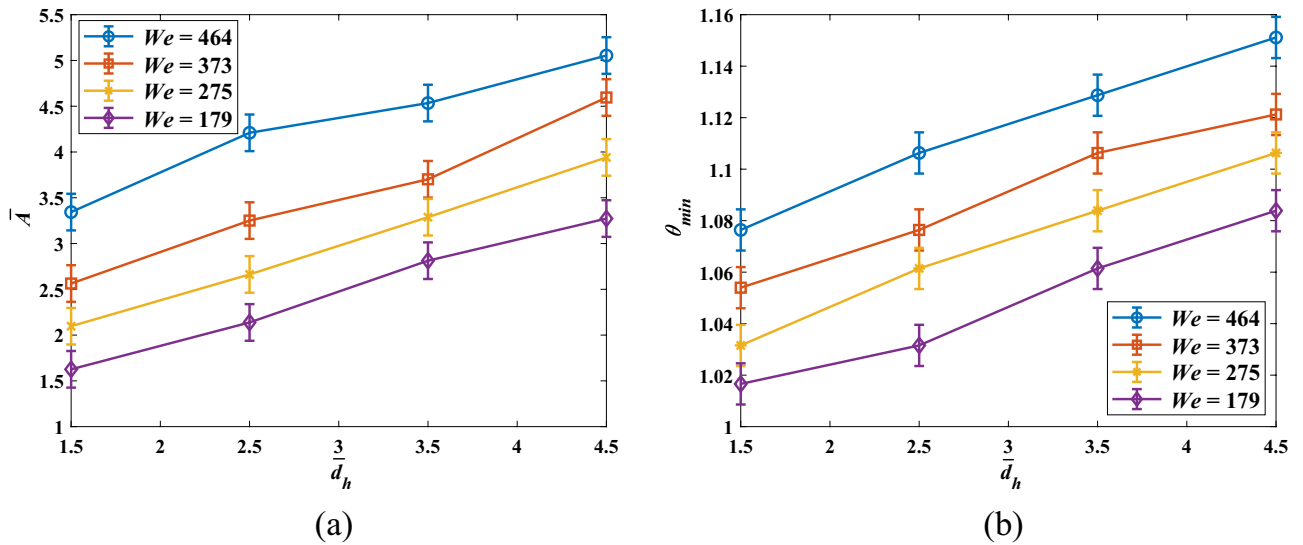


Figure 14. Variation of non-dimensional area (\bar{A}) and dimensionless minimum pool temperature value (θ_{min}) against \bar{d}_h for disparate We numbers at $T = 90^\circ\text{C}$; (a) $\bar{A}(\bar{d}_h)$, and (b) $\theta_{min}(\bar{d}_h)$.

ANN and modeling

An artificial neural network (ANN) is a biologically-inspired computational model featuring numerous computational elements known as "neurons"⁴⁸. In fact, ANN is a programming approach that acquires knowledge by observing data patterns. Initially, a collection of interconnected neurons is established to facilitate communication among them. Subsequently, a problem is formulated to be addressed by the network. The network undergoes iterative processes in an attempt to solve the problem and identify the correlation between input and output data. During the process, the network endeavors to minimize the error between the predicted and exact values. Eventually, by repeating this process, and with the help of thorough training examples and advanced computational power, ANN is capable of providing respond to various inquiries. The architecture of ANN comprises three layers, namely input, hidden, and output. It is worth mentioning that ANN has attracted the attention of researchers regarding modeling, predicting, or optimization problems such as optimizing energy systems, owing to its efficient capability in simulating and modeling nonlinear processes⁴⁹.

Obtained in Section "Experimental results", the experimental values of T_{min} and A are considered as the inputs to the modeling problem serving as training data for the ANN. The trained network is then integrated into the multi-objective NSGA-II algorithm as a fitted function to perform MOO. In this regard, to evaluate the precision of the network in producing output results, a mean squared error (MSE) coefficient is utilized. Figure 15 represents the optimization methodology coupling the experimental and the neural network, as well as the neural network and NSGA-II. To train the network, the two variables of solidified PCM area and minimum pool temperature value after the impact ought to be dimensionless. By using the initial droplet diameter (D) and the paraffin phase change point, the aforementioned variables were nondimensionalized as follows⁴⁴:

$$\bar{A} = \frac{A}{\pi D^2}, D = 2.68\text{mm} \tag{6}$$

$$\theta_{min} = \frac{T_{min}}{T_s}, T_s = 66.89^\circ\text{C}$$

Also, the ranges at which design parameters vary are listed in Table 5.

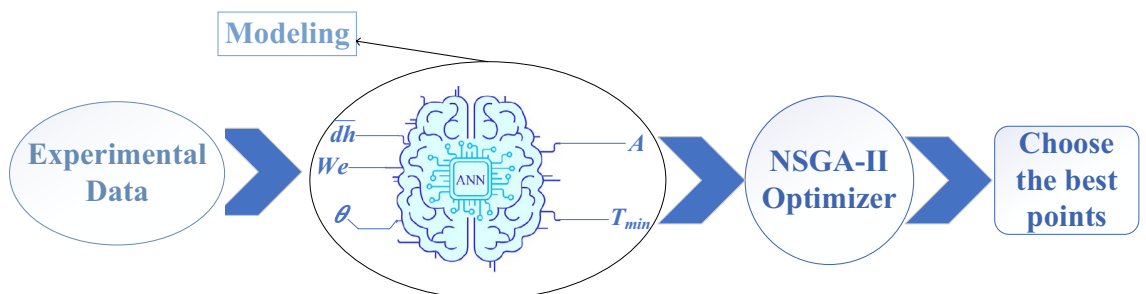


Figure 15. Flowchart of the modeling and optimization methodology.

Design parameters	bounds
\bar{d}_h	1–5
θ	1–2
We	100–1000

Table 5. The range of the input variables changes.

Parameters	Value
Validation percentage	15%
Testing percentage	15%
Number of hidden layers	1
Number of hidden neurons	10
Training function	Levenberg–Marquardt
Validation checks	6

Table 6. Variables used for dimensionless solidified PCM area's neural network.

Identical to ANN, the function fitting neural network (FFNN) bears three layers. The initial point of connection begins with the inputs, and each subsequent layer is linked to the preceding one, ultimately resulting in the production of the output layer⁴⁹. The performance of the network is contingent upon the number of hidden neurons. The optimization of this number is achieved through a process of trial and error. Furthermore, two neural networks were trained to improve the accuracy of modeling for optimization purposes for \bar{A} and θ_{\min} . Table 6 presents the neural network specifications applied to model the dimensionless solidified PCM area. For the purpose of training and testing the network, the data should be divided into three distinct datasets, including training, validation, and testing. During training, it is this set of data used to detect hidden features or patterns in the data. In each epoch, the model learns the features of the training data by feeding it the same training data repeatedly. At the same time, validation sets, separate from training sets, are used to validate the model during training. This validation process provides information that can be used to fine-tune the model's hyperparameters and configurations and determine whether the training is progressing in the right direction. The model is trained on the training set while being evaluated on the validation set at the end of each epoch, preventing the model from overfitting. A test set is then used to test the model's accuracy once it has been trained, providing an unbiased measure of the model's performance. In this concern, 15% of the data is used for validation, 15% for testing, and the rest for training. Furthermore, since the dataset is not noisy, Levenberg–Marquardt's algorithm is employed in the current scholarship. According to this algorithm, training stops automatically when generalization does not improve, as shown by increasing the mean square error of validation samples.

By using the abovementioned parameter variables, the neural network was trained. Figures 16, 17 and 18 depict the neural network analysis of \bar{A} . According to Table 6 and Fig. 16, the validation process undergoes changes after 13 iterations, and the validation increment comes to a halt at iteration 19 to prevent overfitting

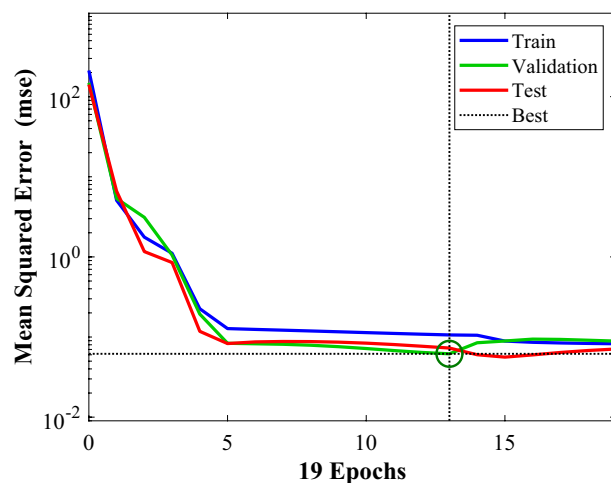


Figure 16. The ANN model's performance during training, testing, and validation for \bar{A} .

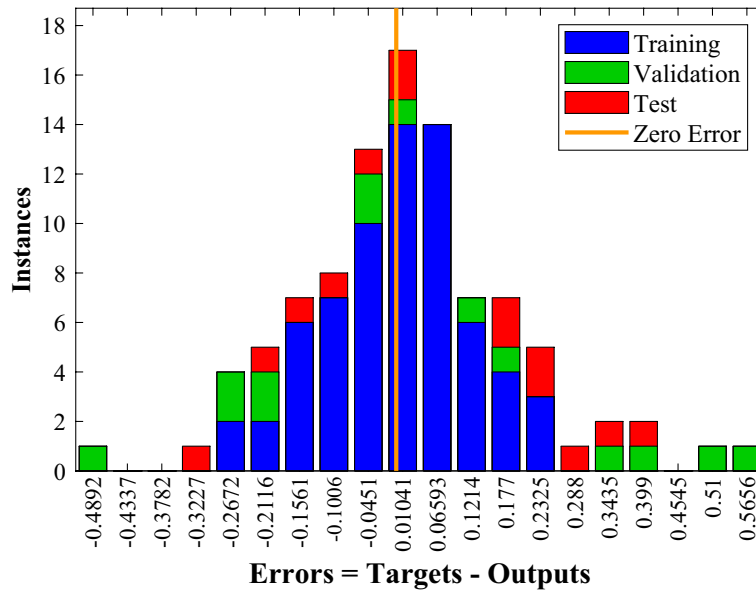


Figure 17. ANN model error histogram for \bar{A} .

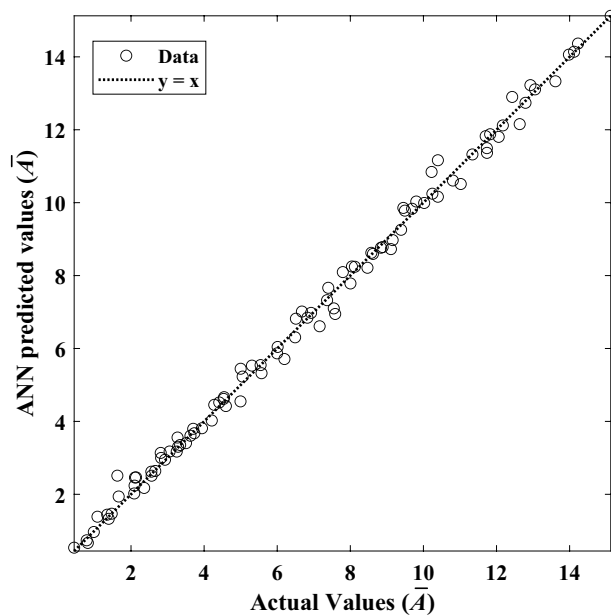


Figure 18. Results of the ANN prediction versus the actual data for \bar{A} .

during neural network iterations. That shows many iterations do not enhance the neural network’s accuracy; in this scenario, iteration 19 is the best value.

Furthermore, Fig. 17 reveals the error histograms generated by the corresponding ANN model providing an exhaustive analysis of the model’s suitability and validity. The average relative error of this network to estimate the amount of \bar{A} is equal to 2%, which indicates the acceptable accuracy of the trained network. In addition, to examine the efficiency of the neural network, the coefficient of determination (R^2) is utilized. It is the value of R^2 that determines how much the output results vary. Figure 18 provides a comparison between the ANN’s output and the exact values. The closer the R^2 value to one, the more accurate the estimate and, hence, the more reliable the trained network. This value for the dimensionless solidified PCM area’s network is 0.98, which denotes high accuracy and reliability.

Another network is utilized to model the dimensionless minimum pool temperature value (θ_{min}) as well. The specifications and parameters that are used in the neural network for θ_{min} are listed in Table 7.

Parameters	Value
Validation percentage	15%
Testing percentage	15%
Number of hidden layers	1
Number of hidden neurons	5
Training function	Levenberg–Marquardt
Validation checks	6

Table 7. Variables used for dimensionless minimum pool temperature’s neural network.

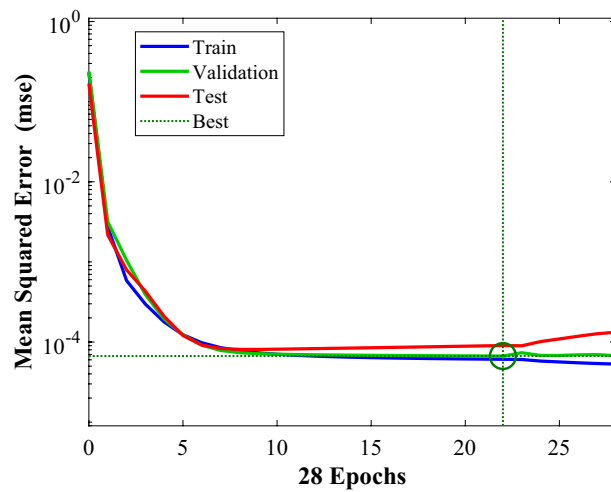


Figure 19. The ANN model’s performance during training, testing, and validation for θ_{\min} .

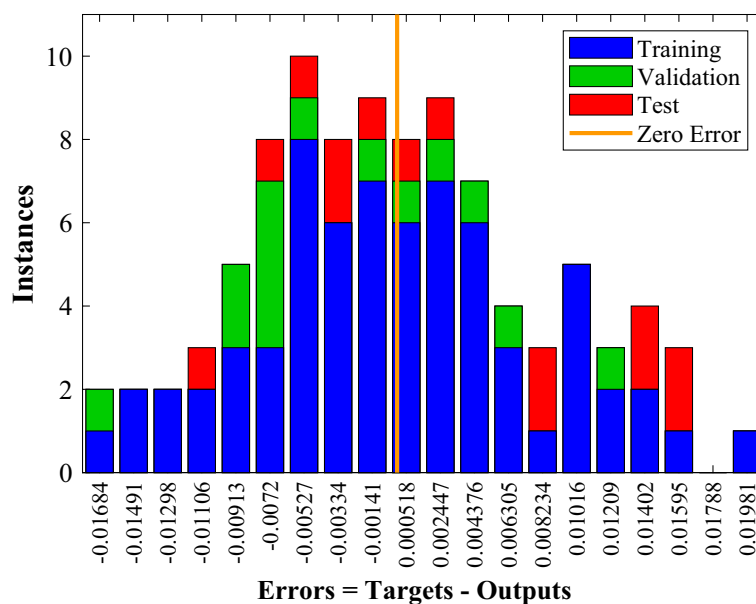


Figure 20. ANN model error histogram for θ_{\min} .

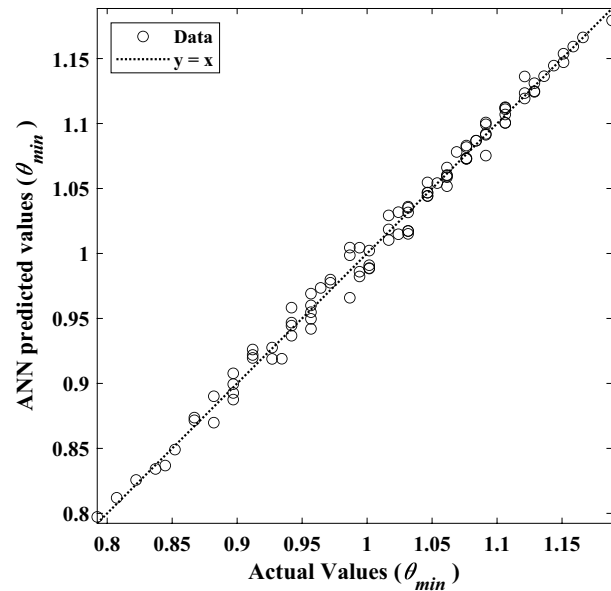


Figure 21. Results of the ANN prediction versus the actual data for θ_{\min} .

Figures 19, 20 and 21 represent the neural network analysis of θ_{\min} . According to Table 6 and Fig. 13, it can be concluded that, as in the previously trained network, the validation increment stops at iteration 28 to prevent overfitting after six iterations. Moreover, Fig. 20 shows the ANN model error histogram for θ_{\min} . According to Fig. 20, the average relative error for this network is 0.9%, demonstrating exceptional accuracy of ANN model. Moreover, based on Fig. 21, the network's coefficient of determination is equal to 0.99, testifying to the high accuracy of the trained network.

Optimization

Optimization is a procedure leading to finding the optimal points of the system to minimize or maximize its performance; as it can be predicted, optimization is of great importance, having rendered many studies to focus on optimizing and designing energy systems to achieve higher performance³². In the meantime, the MOO approach is considered an efficient means of addressing real problems since systems in the real world usually contain several objective functions that are inconsistent with one another⁵⁰. Real-world problems can have constraints and, in some cases, nonlinear objective functions, making them overly challenging to be solved. The mathematical representation of a MOO can be described as follows⁵¹:

$$F(x) = [F_1(x), F_2(x), \dots, F_k(x)]^T \quad (7)$$

which is subjected to:

$$\begin{aligned} G_p(x) &= 0 \forall p = 1, 2, \dots, P \\ H_q(x) &\leq 0 \forall q = 1, 2, \dots, Q \end{aligned} \quad (8)$$

in which the decision parameter vector is represented as x , and k indicates the count of objective functions. Equality and inequality constraints are represented by $G_p(x)$ and $H_q(x)$, respectively. Additionally, P and Q are the parity and constraint numbers, respectively³². Unlike single-objective optimization, in MOO problems, attaining a single optimal solution is impossible. Therefore, the Pareto optimal solution can be used. There is a concept called a non-dominant solution in solving MOO problems. In this case, a candidate solution for a MOO problem is referred to as a non-dominated solution when it improves the values generated by one or more objective functions of the problem while diminishing the quality of the values generated by other objective functions. These answers are known as "Pareto optimal solutions," which are equally suitable and considered as equal. For the purpose of optimizing several objective functions, in this research, the NSGA-II algorithm, an evolved genetic algorithm, is utilized due to its high efficiency and effectiveness in handling multi-objective problems. This is attributed to its fast crowded distance estimation strategy and non-dominated sorting procedure⁵². Figure 22 illustrates the schematic of the NSGA-II algorithms flowchart.

The ideal point (utopia) in optimization problems is where all the objective functions are in the most optimal possible state, and the non-ideal point is where all the objective functions are in the most non-optimal state. These points actually define the upper and lower limits. By considering these points, methods based on the final decision-makers (FDMs) can be used to overcome the problem of not providing a single optimal point in MOO

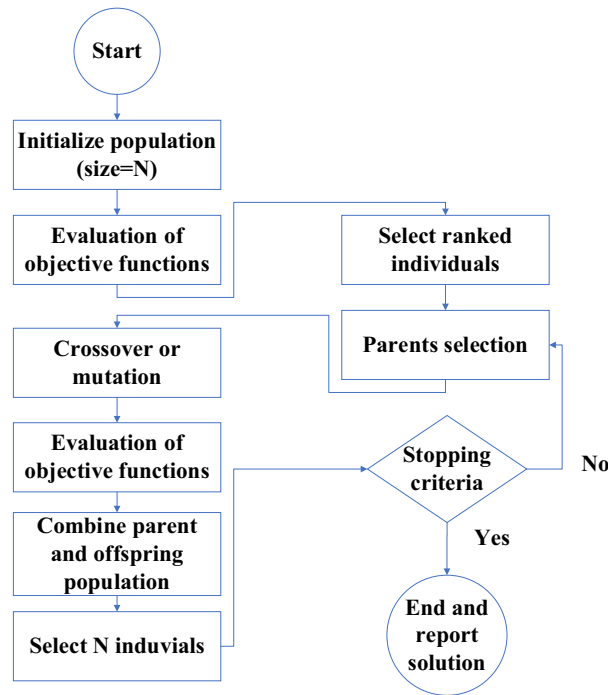


Figure 22. schematic of the NSGA-II flowchart⁵³.

problems. Herein, to attain a single optimal point on the Pareto frontier, two methods, the Linear programming technique for multi-dimensional analysis of performance (LINMAP) and the technique of order preference by similarity to an ideal solution (TOPSIS) are used. The governing equations of the LINMAP method are given as follows⁵³:

$$ED_{i+} = \sqrt{\sum_{s=1}^k (F_{is} - F_S^{ideal})^2} \quad \forall i = 1, 2, \dots, R \quad (9)$$

$$i_{final} = i \in \min(ED_{i+})$$

here, R signifies the quantity of Pareto optimal solutions, while k represents the total number of objective functions. Equation (9) can be obtained by measuring the distance of each Pareto front point from the ideal point based on its Euclidean distance, while in the TOPSIS approach, in addition to considering the distance of the points from the ideal point, the distance from the non-ideal point is also taken into account. Thus, the TOPSIS method determines the closest point to the ideal point and the greatest distance from the non-ideal point with the following equations⁵³:

$$ED_{i-} = \sqrt{\sum_{s=1}^k (F_{is} - F_S^{non-ideal})^2} \quad \forall i = 1, 2, \dots, R \quad (10)$$

$$ED = \frac{ED_{i-}}{ED_{i-} + ED_{i+}}$$

$$i_{final} = i \in \max(ED)$$

where k and R are defined previously. Regarding Section "Experimental results", the parameters governing multiple droplet impact are the Weber number (We), paraffin temperature (T), and the impact spacing (d_h). Therefore, these three variables are considered optimization parameters of the MOO problem. The objective functions of the problem are \bar{A} and θ_{min} as well. As pointed out previously, this research aims to maximize \bar{A} while minimizing θ_{min} so that each droplet impact leads to a large stable solid, which lessens the charge and discharge process. Figure 23 shows the Pareto front diagram of two-objective optimization by considering the mentioned objective functions.

Table 8 provides the results of MOO at the LINMAP and TOPSIS points.

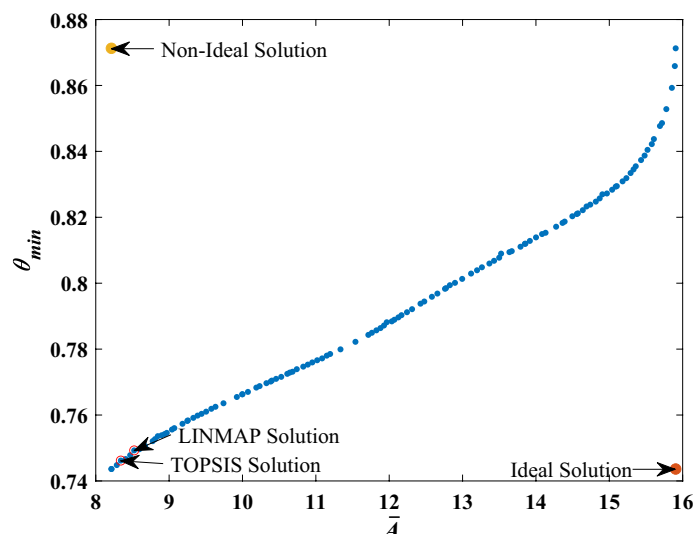


Figure 23. The Pareto front of the objective functions.

FDM	\bar{A}	θ_{min}	We	θ	\bar{d}_h
LINMAP	8.524	0.749	309.444	1.000	1.061
TOPSIS	8.341	0.746	294.978	1.000	1.039

Table 8. Ultimate optimum solutions procured by MOO.

In Fig. 24, scatter distributions are displayed for various design parameters, showcasing the ideal range for the primary decision variables. As can be seen from Fig. 24, the large proportion of optimum points of nondimensionalized temperatures (θ) is in the range of $1.003 < \theta < 1.005$, and the horizontal distance is in the range of $1 < \bar{d}_h < 1.2$ as well. Nonetheless, the optimal points of We numbers are distributed across the entire range of 250–700.

Conclusion

The multi-objective optimization (MOO) of a thermal energy storage (TES) unit working based on the direct contact of heat transfer fluid droplets (ethanol) and a phase change material (paraffin wax) was conducted for the first time. To carry out optimization, solidified PCM area (A) and minimum pool temperature value after the impact (T_{min}) were considered as objective functions. Weber number (We), impact spacing (d_h), and PCM pool temperature (T) have an outstanding effect on objective functions. Initially, experiments were implemented for $179 \leq We \leq 464$, $4.02 \leq d_h \leq 12.06$ mm, and $70 \leq T \leq 95^\circ\text{C}$. By altering impact parameters, a great amount of objective functions data was obtained employing high-speed and IR imaging as well as image post-processing. Subsequently, exploiting the artificial neural network (ANN), two models were fitted to each of the objective functions. In addition, it was shown that the accuracy and reliability of suggested models are excellent. Afterward, the trained networks were given to the multi-objective non-dominated sorting genetic algorithm II (NSGA-II) to perform multi-objective (MOO) optimization. Ultimately, through two disparate decision-making methods (FDMs), the optimum impact conditions were accomplished. The pivotal outcomes of the study can be recapitulated as follows:

- Diminishing the PCM pool temperature results in a greater solidified area and a lower T_{min} ; both of which are advantageous to TES.
- While enhancing A , the increment of the We number raises T_{min} . Accordingly, one should fulfill a trade-off between A and T_{min} when determining the Weber number.
- A decrement in horizontal spacing instigates a lower T_{min} , while providing a smaller solidified area, entailing a trade-off between A and T_{min} during characterizing horizontal impact spacing.
- Final ideal solutions were obtained by LINMAP ($We = 309.44$, $\bar{d}_h = 1.06$, $\theta = 1.00$) and TOPSIS ($We = 294.98$, $\bar{d}_h = 1.04$, $\theta = 1.00$) from the Pareto front diagram.
- The maximum solidified PCM area determined by LINMAP and TOPSIS equals 192.34mm^2 and 188.21mm^2 , respectively.
- The minimum pool temperature values attained by LINMAP and TOPSIS are 50.10°C and 49.90°C , respectively.

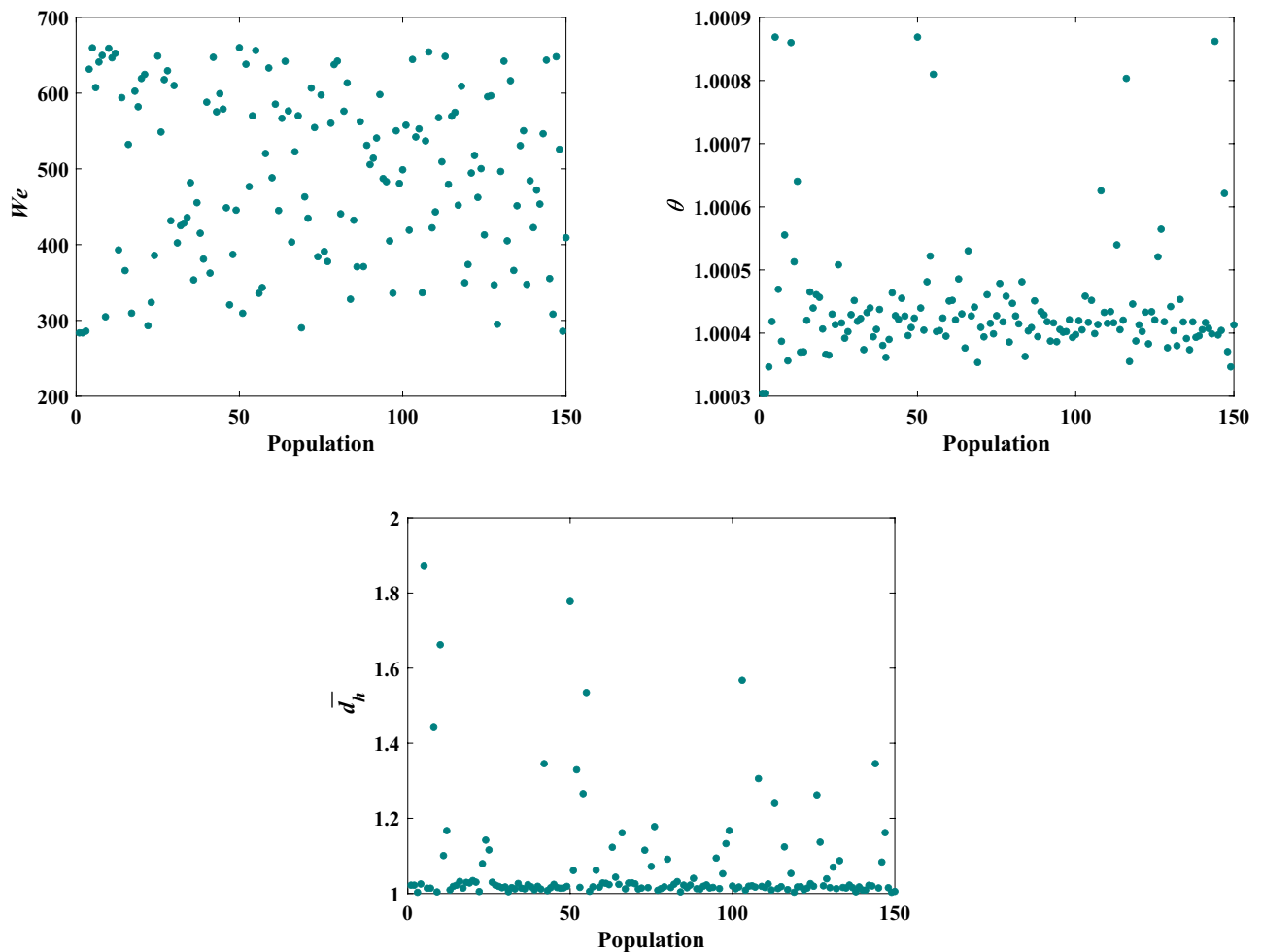


Figure 24. Scatter distribution of design parameters.

Data availability

The datasets generated during and/or analyzed during the current study are available from the corresponding author on reasonable request.

Received: 17 February 2023; Accepted: 26 June 2023

Published online: 29 June 2023

References

- Li, Z.-R., Hu, N. & Fan, L.-W. Nanocomposite phase change materials for high-performance thermal energy storage: A critical review. *Energy Storage Mater.* <https://doi.org/10.1016/j.ensm.2022.12.037> (2022).
- Jančík, P. *et al.* Constant mixing temperature test of a fin-and-tube latent heat thermal energy storage. *Sci. Rep.* **12**, 20961. <https://doi.org/10.1038/s41598-022-24990-0> (2022).
- Ahmed, S. *et al.* Melting enhancement of PCM in a finned tube latent heat thermal energy storage. *Sci. Rep.* **12**, 11521. <https://doi.org/10.1038/s41598-022-15797-0> (2022).
- Liu, J., Xu, J., Su, Z., Zhang, Y. & Jiang, T. Preparation and characterization of NaNO₃ shape-stabilized phase change materials (SS-PCMs) based on anorthite ceramic and cordierite ceramic for solar energy storage. *Solar Energy Mater. Solar Cells* **251**, 112114. <https://doi.org/10.1016/j.solmat.2022.112114> (2023).
- Bre, F., Lamberts, R., Flores-Larsen, S. & Koenders, E. A. B. Multi-objective optimization of latent energy storage in buildings by using phase change materials with different melting temperatures. *Appl. Energy* **336**, 120806. <https://doi.org/10.1016/j.apenergy.2023.120806> (2023).
- Ma, Y. *et al.* Energy and daylighting performance of a building containing an innovative glazing window with solid-solid phase change material and silica aerogel integration. *Energy Convers. Manag.* **271**, 116341. <https://doi.org/10.1016/j.enconman.2022.116341> (2022).
- Sadeghi, K. *et al.* Towards net-zero emissions through the hybrid SMR-solar cogeneration plant equipped with modular PCM storage system for seawater desalination. *Desalination* **524**, 115476. <https://doi.org/10.1016/j.desal.2021.115476> (2022).
- Bianco, V., De Rosa, M. & Vafai, K. Phase-change materials for thermal management of electronic devices. *Appl. Therm. Eng.* **214**, 118839. <https://doi.org/10.1016/j.applthermaleng.2022.118839> (2022).
- Liu, A., Lin, J. & Zhuang, Y. PIV experimental study on the phase change behavior of phase change material with partial filling of metal foam inside a cavity during melting. *Int. J. Heat Mass Transf.* **187**, 122567. <https://doi.org/10.1016/j.ijheatmasstransfer.2022.122567> (2022).

10. Wang, K., Yan, T., Zhao, Y. M., Li, G. D. & Pan, W. G. Preparation and thermal properties of palmitic acid @ZnO/Expanded graphite composite phase change material for heat storage. *Energy* **242**, 122972. <https://doi.org/10.1016/j.energy.2021.122972> (2022).
11. Li, Y. *et al.* Experimental study on preparation and thermal storage properties of expanded graphite/paraffin wax as a shape-stabilized phase change material. *Energy Rep.* **8**, 324–331. <https://doi.org/10.1016/j.egyrr.2022.09.149> (2022).
12. Almarashi, A., Hussin, A. M., Mirparizi, M., Zhang, C. & Saad, H. A. Influence of nanoparticles on freezing inside container equipped with fins. *Sci. Rep.* **12**, 14792. <https://doi.org/10.1038/s41598-022-18714-7> (2022).
13. Al-Ahmed, A. *et al.* Thermal energy storage and thermal conductivity properties of Octadecanol-MWCNT composite PCMs as promising organic heat storage materials. *Sci. Rep.* **10**, 9168. <https://doi.org/10.1038/s41598-020-64149-3> (2020).
14. NematpourKeshтели, A., Iasiello, M., Langella, G. & Bianco, N. Enhancing PCMs thermal conductivity: A comparison among porous metal foams, nanoparticles and finned surfaces in triplex tube heat exchangers. *Appl. Therm. Eng.* **212**, 118623. <https://doi.org/10.1016/j.applthermaleng.2022.118623> (2022).
15. Cui, W. *et al.* Combined effects of nanoparticles and ultrasonic field on thermal energy storage performance of phase change materials with metal foam. *Appl. Energy* **309**, 118465. <https://doi.org/10.1016/j.apenergy.2022.118465> (2022).
16. Faghiri, S., Mohammadi, O., Hosseiniaveh, H. & Shafii, M. B. The impingement of liquid boiling droplet onto a molten phase change material as a direct-contact solidification method. *Therm. Sci. Eng. Progress* **23**, 100888. <https://doi.org/10.1016/j.tsep.2021.100888> (2021).
17. Martin, V., He, B. & Setterwall, F. Direct contact PCM–water cold storage. *Appl. Energy* **87**, 2652–2659. <https://doi.org/10.1016/j.apenergy.2010.01.005> (2010).
18. Hegner, L. *et al.* Experimental feasibility study of a direct contact latent heat storage using an ester as a bio-based storage material. *Energies* **14**, 511. <https://doi.org/10.3390/en14020511> (2021).
19. Al Omari, S. A. B., Ghazal, A. M., Elnajjar, E. & Qureshi, Z. A. Vibration-enhanced direct contact heat exchange using gallium as a solid phase change material. *Int. Commun. Heat Mass Transf.* **120**, 104990. <https://doi.org/10.1016/j.icheatmasstransfer.2020.104990> (2021).
20. Hosseiniaveh, H., Mohammadi, O., Faghiri, S. & Shafii, M. B. A comprehensive study on the complete charging–discharging cycle of a phase change material using intermediate boiling fluid to control energy flow. *J. Energy Storage* **35**, 102235. <https://doi.org/10.1016/j.est.2021.102235> (2021).
21. Ramazani, H. Z., Mohammadi, O., Rahgozar, I., Shafii, M. B. & Ahmadi, M. H. Super-fast discharge of phase change materials by using an intermediate boiling fluid. *Int. Commun. Heat Mass Transf.* **115**, 104597. <https://doi.org/10.1016/j.icheatmasstransfer.2020.104597> (2020).
22. Guo, Z., Zhang, W., Jin, S., Shi, Z. & Yuan, Y. Experimental investigation of heat transfer for diesel spray impingement on a high temperature wall. *Sci. Rep.* **12**, 6771. <https://doi.org/10.1038/s41598-022-10959-6> (2022).
23. Santangelo, P. E., Romagnoli, M. & Puglia, M. An experimental approach to evaluate drying kinetics and foam formation in inks for inkjet printing of fuel-cell layers. *Exp. Therm. Fluid Sci.* **135**, 110631. <https://doi.org/10.1016/j.expthermflusci.2022.1106314> (2022).
24. Zhang, C., Li, L., Li, Z., Chang, H. & Liu, J. Investigation on the spreading and solidification of supercooled gallium droplets during impact. *Int. J. Heat Mass Transf.* **183**, 122142. <https://doi.org/10.1016/j.ijheatmasstransfer.2021.122142> (2022).
25. Zhan, L. *et al.* Molecular dynamics study on evaporation of high-salinity wastewater droplet. *Appl. Therm. Eng.* **213**, 118752. <https://doi.org/10.1016/j.applthermaleng.2022.118752> (2022).
26. Liang, G., Yu, H., Chen, L. & Shen, S. Interfacial phenomena in impact of droplet array on solid wall. *Acta Mech.* **231**, 305–319. <https://doi.org/10.1007/s00707-019-02542-4> (2020).
27. Guggilla, G., Pattamatta, A. & Narayanaswamy, R. Numerical investigation into the evaporation dynamics of drop-on-drop collisions over heated wetting surfaces. *Int. J. Heat Mass Transf.* **123**, 1050–1067. <https://doi.org/10.1016/j.ijheatmasstransfer.2018.03.029> (2018).
28. Guilizzoni, M., Santini, M. & Fest-Santini, S. Synchronized multiple drop impacts into a deep pool. *Fluids* **4**, 141. <https://doi.org/10.3390/fluids4030141> (2019).
29. Goswami, A. & Hardalupas, Y. Simultaneous impact of droplet pairs on solid surfaces. *J. Fluid Mech.* **961**, A17. <https://doi.org/10.1017/jfm.2023.249> (2023).
30. Kirar, P. K., Pokale, S. D., Sahu, K. C., Ray, B. & Biswas, G. Influence of the interaction of capillary waves on the dynamics of two drops falling side-by-side on a liquid pool. *Phys. Fluids* **34**, 112114. <https://doi.org/10.1063/5.0121615> (2022).
31. Kasem, M. M. Multiobjective design optimization of parabolic trough collectors. *Sci. Rep.* **12**, 19964. <https://doi.org/10.1038/s41598-022-24305-3> (2022).
32. Faghiri, S., Aria, H. P. & Shafii, M. B. Multi-objective optimization of acetone droplet impingement on phase change material in direct-contact discharge method. *J. Energy Storage* **46**, 103862. <https://doi.org/10.1016/j.est.2021.103862> (2022).
33. Khalkhali, A., Sadafi, M., Rezapour, J. & Safikhani, H. Pareto based multi-objective optimization of solar thermal energy storage using genetic algorithms. *Trans. Can. Soc. Mech. Eng.* **34**, 463–474. <https://doi.org/10.1139/tcsme-2010-0028> (2010).
34. Zhang, C., Zhang, X., Qiu, L. & Zhao, Y. Multi-objective optimization of a latent thermal energy storage unit with compound enhancement method. *Appl. Therm. Eng.* **181**, 115736. <https://doi.org/10.1016/j.applthermaleng.2020.115736> (2020).
35. Lin, W., Ma, Z., Ren, H., Gschwander, S. & Wang, S. Multi-objective optimisation of thermal energy storage using phase change materials for solar air systems. *Renew. Energy* **130**, 1116–1129. <https://doi.org/10.1016/j.renene.2018.08.071> (2019).
36. Huang, S., Ma, Z. & Wang, F. A multi-objective design optimization strategy for vertical ground heat exchangers. *Energy Build.* **87**, 233–242. <https://doi.org/10.1016/j.enbuild.2014.11.024> (2015).
37. Liang, H., Niu, J. & Gan, Y. Performance optimization for shell-and-tube PCM thermal energy storage. *J. Energy Storage* **30**, 101421. <https://doi.org/10.1016/j.est.2020.101421> (2020).
38. Peng, B., He, Z., Wang, H. & Su, F. Optimization of patterned-fins for enhancing charging performances of phase change materials-based thermal energy storage systems. *Int. J. Heat Mass Transf.* **164**, 120573. <https://doi.org/10.1016/j.ijheatmasstransfer.2020.120573> (2021).
39. Li, Y., Ding, Z., Shakerin, M. & Zhang, N. A multi-objective optimal design method for thermal energy storage systems with PCM: A case study for outdoor swimming pool heating application. *J. Energy Storage* **29**, 101371. <https://doi.org/10.1016/j.est.2020.101371> (2020).
40. Moon, J. H., Lee, K. H., Han, D. I. & Lee, C.-H. Cooling performance enhancement study of single droplet impingement on heated hole-patterned surfaces using improved GQPSO algorithm. *Case Stud. Therm. Eng.* **41**, 102679. <https://doi.org/10.1016/j.csite.2022.102679> (2023).
41. Poureslami, P., Faghiri, S. & Shafii, M. B. Simultaneous double droplet impact on a molten phase change material pool: An experimental investigation. *Phys. Fluids* **35**, 027110. <https://doi.org/10.1063/5.0132570> (2023).
42. Lee, Y. *et al.* Symmetry breaking of Worthington jets by gradients in liquid pool depth. *Phys. Fluids* **32**, 112104. <https://doi.org/10.1063/5.0028067> (2020).
43. Das, S. K., Dalal, A., Breuer, M. & Biswas, G. Evolution of jets during drop impact on a deep liquid pool. *Phys. Fluids* **34**, 022110. <https://doi.org/10.1063/5.0081064> (2022).
44. Gultekin, A., Erkan, N., Ozdemir, E., Colak, U. & Suzuki, S. Simultaneous multiple droplet impact and their interactions on a heated surface. *Exp. Therm. Fluid Sci.* **120**, 110255. <https://doi.org/10.1016/j.expthermflusci.2020.110255> (2021).

45. Basu, A. S. Droplet morphometry and velocimetry (DMV): A video processing software for time-resolved, label-free tracking of droplet parameters. *Lab Chip* **13**, 1892–1901. <https://doi.org/10.1039/C3LC50074H> (2013).
46. Ho, C. J., Peng, J.-K., Yang, T.-F., Rashidi, S. & Yan, W.-M. On the assessment of the thermal performance of microchannel heat sink with nanofluid. *Int. J. Heat Mass Transf.* **201**, 123572. <https://doi.org/10.1016/j.ijheatmasstransfer.2022.123572> (2023).
47. Zhang, T., Alvarado, J. L., Muthusamy, J. P., Kanjirakat, A. & Sadr, R. Heat transfer characteristics of double, triple and hexagonally-arranged droplet train impingement arrays. *Int. J. Heat Mass Transf.* **110**, 562–575. <https://doi.org/10.1016/j.ijheatmasstransfer.2017.03.009> (2017).
48. Agatonovic-Kustrin, S. & Beresford, R. Basic concepts of artificial neural network (ANN) modeling and its application in pharmaceutical research. *J. Pharm. Biomed. Anal.* **22**, 717–727. [https://doi.org/10.1016/S0731-7085\(99\)00272-1](https://doi.org/10.1016/S0731-7085(99)00272-1) (2000).
49. Alirahmi, S. M., Mousavi, S. F., Ahmadi, P. & Arabkoohsar, A. Soft computing analysis of a compressed air energy storage and SOFC system via different artificial neural network architecture and tri-objective grey wolf optimization. *Energy* **236**, 121412. <https://doi.org/10.1016/j.energy.2021.121412> (2021).
50. Shirazi, A., Taylor, R. A., Morrison, G. L. & White, S. D. A comprehensive, multi-objective optimization of solar-powered absorption chiller systems for air-conditioning applications. *Energy Convers. Manage.* **132**, 281–306. <https://doi.org/10.1016/j.enconman.2016.11.039> (2017).
51. Marler, R. T. & Arora, J. S. Survey of multi-objective optimization methods for engineering. *Struct. Multidiscip. Optim.* **26**, 369–395. <https://doi.org/10.1007/s00158-003-0368-6> (2004).
52. Deb, K., Pratap, A., Agarwal, S. & Meyarivan, T. A fast and elitist multiobjective genetic algorithm: NSGA-II. *IEEE Trans. Evol. Comput.* **6**, 182–197. <https://doi.org/10.1109/4235.996017> (2002).
53. Yao, Q. Multi-objective optimization design of spur gear based on NSGA-II and decision making. *Adv. Mech. Eng.* **11**, 1687814018824936. <https://doi.org/10.1177/1687814018824936> (2019).

Acknowledgements

The authors are grateful to the Deputy of Research and Technology of Sharif University of Technology and Sharif Energy, Water and Environment Institute (SEWEI) for providing an appropriate working environment to conduct the research.

Author contributions

S.F. and P.P. designed the research and conducted the experiments. H.P. performed optimization and prepared the results. S.F., P.P., and H.P. analyzed the results. P.P., S.F. and H.P. wrote the original draft. M.B.S. critically reviewed the manuscript and supervised the project.

Competing interests

The authors declare no competing interests.

Additional information

Correspondence and requests for materials should be addressed to M.B.S.

Reprints and permissions information is available at www.nature.com/reprints.

Publisher's note Springer Nature remains neutral with regard to jurisdictional claims in published maps and institutional affiliations.



Open Access This article is licensed under a Creative Commons Attribution 4.0 International License, which permits use, sharing, adaptation, distribution and reproduction in any medium or format, as long as you give appropriate credit to the original author(s) and the source, provide a link to the Creative Commons licence, and indicate if changes were made. The images or other third party material in this article are included in the article's Creative Commons licence, unless indicated otherwise in a credit line to the material. If material is not included in the article's Creative Commons licence and your intended use is not permitted by statutory regulation or exceeds the permitted use, you will need to obtain permission directly from the copyright holder. To view a copy of this licence, visit <http://creativecommons.org/licenses/by/4.0/>.

© The Author(s) 2023